东南大学图书馆
Southeast University Library

# 东图学术快报
## Academic express of SEU LIB

前沿经典　学科热点

学术动态　工具助手

**编者按：**2021 年不仅是“十四五”的开局之年，也是两个百年目标交汇与转换之年。为了让我校师生快速了解国内外学术前沿、经典及热点，图书馆学科服务团队特开辟此栏目，利用 WOS/ESI/Incites、Scopus/SciVal 等权威数据库和分析工具筛选研究前沿，或跟踪重要学术网站获取最新学术动态，分专题进行编译报道。我们也面向全校师生征集关注的领域和专题。

本期推荐报道 Nature、Science 期刊上材料科学领域的最新论文。



CONTACT US

联系电话：025-52090336-817

办公地址：李文正图书馆 B401 室

编辑：刘丽娟

审核：陆　美

美国 Science(《科学》)、英国 Nature(《自然》)及美国 Cell(《细胞》)是国际公认的三大享有最高学术声誉的科技期刊，发表在这三大期刊上的论文简称 CNS 论文。本次精选 2021 年 10 月 Science 和 Nature 中的部分材料科学领域论文，详细情况如下。

## 材料科学 10 月 Science 论文

[1] **Electrically switchable metallic polymer nanoantennas**

电切换金属聚合物纳米天线

**出版信息：**SCIENCE 29 Oct 2021，Vol 374, Issue 6567，pp. 612-616

**作者：**JULIAN KARST, MORITZ FLOESS, MONIKA UBL, CARSTEN DINGLER, CLAUDIA MALACRIDA, TOBIAS STEINLE, ET AL.

**第一作者单位：**4th Physics Institute and Research Center SCoPE,University of Stuttgart, Pfaffenwaldring 57, 70569 Stuttgart,Germany.

**全文链接：**https://www.science.org/doi/10.1126/science.abj3433

**Abstract：**

Electrical switching of a metal-to-insulator transition would provide a building block for integrated electro-optically active plasmonics. In this work, we realize plasmonic nanoantennas from metallic polymers, which show well-pronounced localized plasmon resonances in their metallic state. As a result of the electrochemically driven optical metal-to-insulator transition of the polymer, the plasmonic resonances can be electrically switched fully off and back on at video-rate frequencies of up to 30 hertz by applying alternating voltages of only ±1 volt. With the use of this concept, we demonstrate electrically switchable beam-steering metasurfaces with a 100% contrast ratio in transmission. Our approach will help to realize ultrahigh efficiency plasmonic-based integrated active optical devices, including high-resolution augmented and virtual reality technologies.

**摘要翻译：**

金属-绝缘体过渡的电切换将为集成电光有源等离子体提供一个构建块。在这项工作中，研究组在金属聚合物中实现了等离子体纳米天线，它们在金属状态下表现出明显的局域等离子体共振。

由于电化学驱动聚合物从光学金属转变为绝缘体，仅通过施加±1 伏的交流电压，等离子体共振即可在高达 30 Hz 的视频速率频率下完全关闭和重新启动。

利用这一概念，研究组演示了在传输中具有 100%对比度的电切换光束控制超表面。该方法将有助于实现基于超高效等离子体的集成有源光学器件，包括高分辨率增强和虚拟现实技术。

**文中插图：**

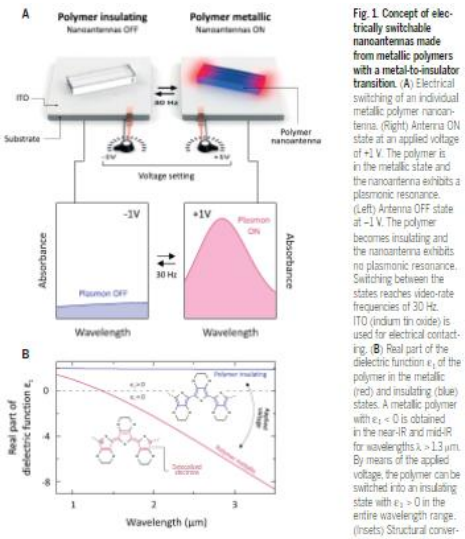


Fig. 1. Concept of electrically switchable nanoantennas made from metallic polymers with a metal-to-insulator transition. (A) Electrical switching of an individual metallic polymer nanoantenna. (Right) Antenna ON state at an applied voltage of +1 V. The polymer is in the metallic state and the nanoantenna exhibits a plasmonic resonance. (Left) Antenna OFF state at −1 V. The polymer becomes insulating and the nanoantenna exhibits no plasmonic resonance. Switching between the states reaches video-rate frequencies of 30 Hz. ITO (indium tin oxide) is used for electrical contacting. (B) Real part of the dielectric function $\varepsilon_1$ of the polymer in the metallic (red) and insulating (blue) states. A metallic polymer with $\varepsilon_1 < 0$ is obtained in the near-IR and mid-IR for wavelengths $\lambda > 1.3$ μm. By means of the applied voltage, the polymer can be switched into an insulating state with $\varepsilon_1 > 0$ in the entire wavelength range. (Insets) Structural conversion of the metal-to-insulator transition.

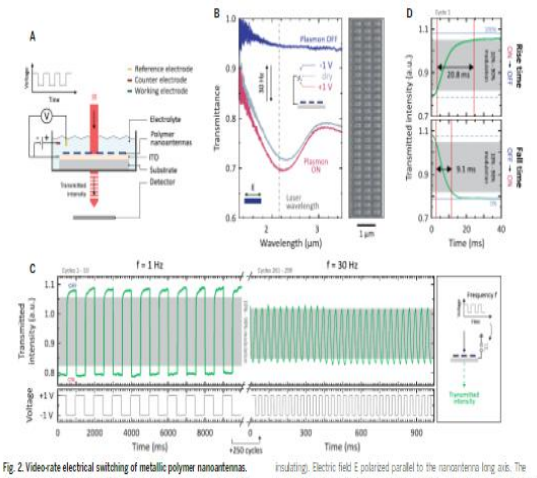


Fig. 2. Video-rate electrical switching of metallic polymer nanoantennas. (A) Schematic of the electrochemical cell (three-electrode setup) and optical measurement setup. (B) SEM image and spectral response of metallic polymer nanoantennas (length $L$ = 300 nm, width $W$ = 160 nm, height $H$ = 90 nm, periodicity in $x$ $P_x$ = 500 nm, periodicity in $y$ $P_y$ = 300 nm) for different states. Dry state, pristine (gray): Plasmonic resonance almost completely turned ON. +1 V (red): Plasmonic resonance completely turned ON with highest modulation (polymer fully metallic). −1 V (blue): Plasmonic resonance turned OFF (polymer insulating). Electric field E polarized parallel to the nanoantenna long axis. The dashed line indicates the laser wavelength $\lambda$ = 2.15 μm for (C) and (D). (C) (Top) Transmitted intensity through the polymer nanoantennas cycling between the ON and OFF states. The gray area denotes the 10% to 90% modulation window. (Bottom) Set voltage switching between +1 V and −1 V. (Left) Cycles 1 to 10 with switching frequency $f$ = 1 Hz. (Right) Cycles 261 to 290 with $f$ = 30 Hz. a.u., arbitrary units. (D) Detailed analysis of rise time $\tau_{rise}$ = 20.8 ms (ON to OFF) and fall time $\tau_{fall}$ = 9.1 ms (OFF to ON) for the first switching cycle.

[2]**Lightweight, strong, moldable wood via cell wall engineering as a sustainable structural material**

**通过细胞壁工程将轻而坚固的可模压木材作为可持续的结构材料**

**出版信息：**SCIENCE 22 Oct 2021，Vol 374, Issue 6566，pp. 465-471

**作者：**SHAOLIANG XIAO, XCHAOJI CHEN, XQINQIN XIA et al.

**第一作者单位：**Department of Materials Science and Engineering, University ofMaryland,CollegePark,MD20742,USA.

**全文链接：**https://www.science.org/doi/10.1126/science.abg9556

**Abstract：**

Wood is a sustainable structural material, but it cannot be easily shaped while maintaining its mechanical properties. We report a processing strategy that uses cell wall engineering to shape flat sheets of hardwood into versatile three-dimensional (3D) structures. After breaking down wood's lignin component and closing the vessels and fibers by evaporating water, we partially re-swell the wood in a rapid water-shock process that selectively opens the vessels. This forms a distinct wrinkled cell wall structure that allows the material to be folded and molded into desired shapes. The resulting 3D-molded wood is six times stronger than the starting wood and comparable to widely used lightweight materials such as aluminum alloys. This approach widens wood's potential as a structural material, with lower environmental impact for buildings and transportation applications.

**摘要翻译：**

木材是一种可持续的结构材料，但它不能在保持机械性能的同时容易塑形。我们报告了一种处理策略，利用细胞壁工程将硬木平面板塑造成通用的三维结构。

在分解木材的木质素成分并通过蒸发水关闭导管和纤维后，我们在快速水冲击过程中部分地重新膨胀木材，选择性地打开导管。

这形成了独特的皱纹细胞壁结构，允许材料折叠并成型为所需的形状。由此产生的 3D 成型木材比起始木材强六倍，可与广泛使用的轻质材料（如铝合金）相媲美。这种方法增加了木材作为结构材料的潜力，降低了对建筑和交通应用的环境影响。

**文中插图：**

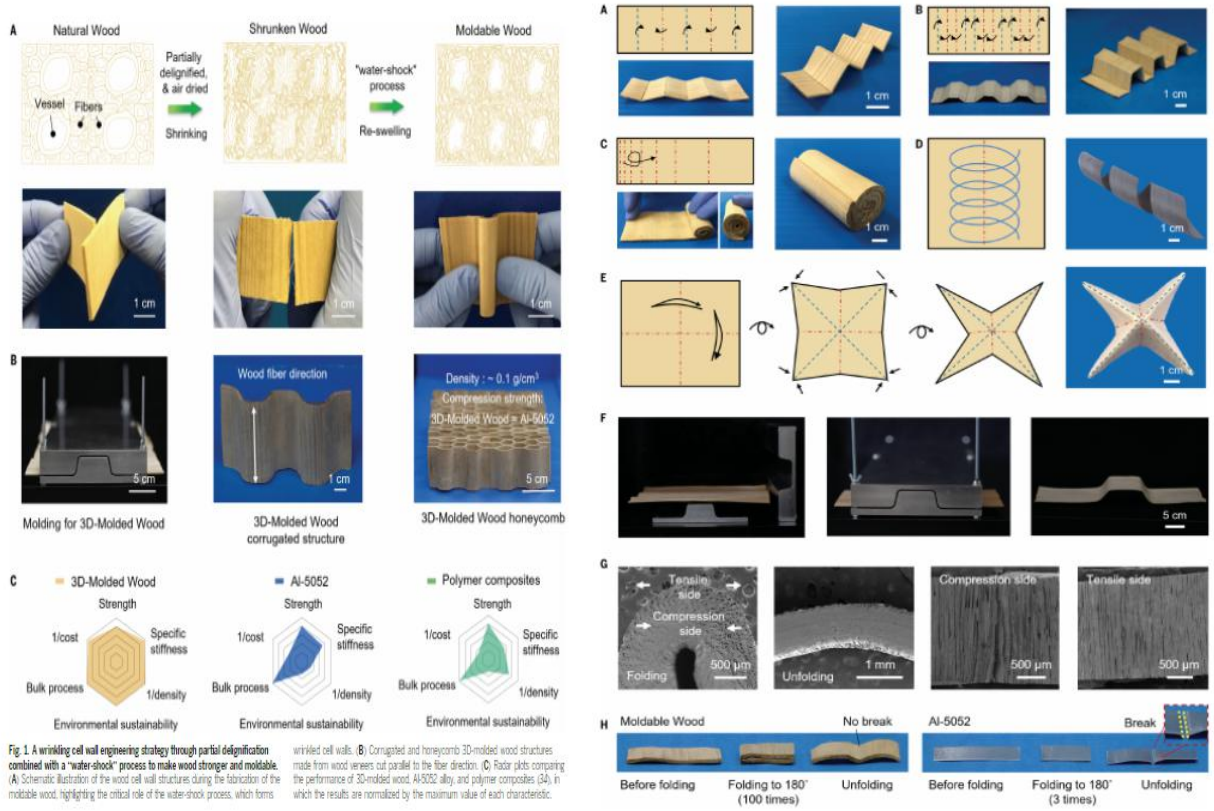


Fig. 1. A wrinkling cell wall engineering strategy through partial delignification combined with a "water-shock" process to make wood stronger and moldable. (A) Schematic illustration of the wood cell wall structures during the fabrication of the moldable wood, highlighting the critical role of the water-shock process, which forms wrinkled cell walls. (B) Corrugated and honeycomb 3D-molded wood structures made from wood veneers cut parallel to the fiber direction. (C) Radar plots comparing the performance of 3D-molded wood, Al-5052 alloy, and polymer composites (34), in which the results are normalized by the maximum value of each characteristic.

[3] **In situ design of advanced titanium alloy with concentration modulations by additive manufacturing**

**利用增材制造设计成分调制钛合金**

**出版信息：**SCIENCE 22 Oct 2021，Vol 374, Issue 6566，pp. 478-482

**作者：**TIANLONG ZHANG, ZHENGHUA HUANG, TAO YANG et al.

**第一作者单位：**Department of Materials Science and Engineering, HongKong Institute for Advanced Study, College of Science andEngineering, City University of Hong Kong, Hong Kong,China

**全文链接：**https://www.science.org/doi/10.1126/science.abj3770

**国内相关报道：**http://news.xjtu.edu.cn/info/1004/172402.htm

**Abstract：**

Additive manufacturing is a revolutionary technology that offers a different pathway for material processing and design. However, innovations in either new materials or new processing technologies can seldom be successful without a synergistic combination. We demonstrate an in situ design approach to make alloys spatially modulated in concentration by using laser-powder bed fusion. We show that the partial homogenization of two dissimilar alloy melts—Ti-6Al-4V and a small amount of 316L stainless steel—allows us to produce micrometer-scale concentration modulations of the elements that are contained in 316L in the Ti-6Al-4V matrix. The corresponding phase stability modulation creates a fine scale–modulated β + α′ dual-phase microstructure that exhibits a progressive transformation-induced plasticity effect, which leads to a high tensile strength of ~1.3 gigapascals with a uniform elongation of ~9% and an excellent work-hardening capacity of >300 megapascals. This approach creates a pathway for concentration-modulated heterogeneous alloy design for structural and functional applications.

**摘要翻译：**

增材制造是一项革命性的技术，为材料加工和设计提供了不同的途径。然而，如果没有协同的组合，新材料或新加工技术的创新很少能成功。我们展示了一种原位设计方法，利用激光粉末床聚变调制合金浓度空间。

我们发现，两种不同合金熔体——Ti-6Al-4V 和少量 316L 不锈钢的部分均匀化，使我们能够对 Ti-6Al-4V 基体中 316L 中所含的元素进行微米级浓度调节。相稳定性以及微观组织形成了α’马氏体和亚稳定β母相在三维空间中的周期性分布及独特微观组织。

亚稳定β相发生明显的相变诱导塑性，从而极大地改善了增材制造钛合金的均匀变形和加工硬化能力。这种方法为结构和功能应用的浓度调制异质合金设计开辟了一条途径。

**文中插图：**

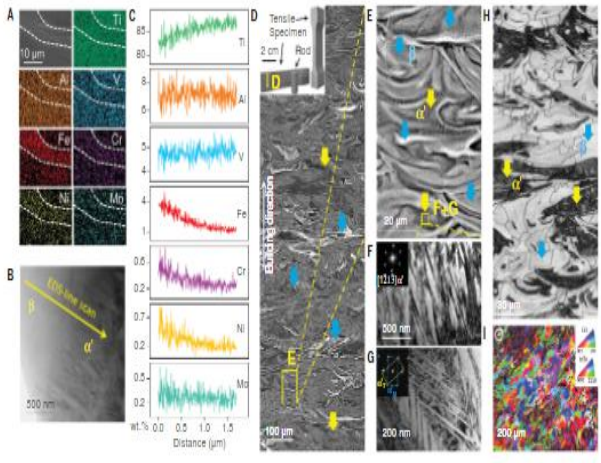

**Fig. 1. Micrometer-scale concentration modulation and microstructures of the as-printed Ti64-(4.5%)316L alloy.** (**A**) SEM-EDS maps showing the micrometer-scale depletion of Ti, Al, and V and enrichment of Fe, Cr, and Ni elements within one of the swirls of the melt pool. (**B**) Scanning TEM image of the β-α′ interphase region. The yellow arrow denotes the EDS line scan direction in (**C**). (**C**) Composition profiles across the β-α′ interphase boundary in (**B**) showing the enrichment of 316L elements (Fe, Cr, Ni, and Mo) in the β phase and depletion of 316L elements in the α′ phase. (**D**) Side-view cross-sectional BSE image showing lava-like microstructure with the clear swirl pattern from Marangoni convection during mechanical mixing in the melt pool. Brighter regions are enriched in heavy elements (Fe, Cr, Ni, and Mo in 316L, blue arrows), and darker regions are enriched in light elements (Ti, Al, and V in Ti64, yellow arrows). The inset shows a photograph of the as-printed Ti64-(4.5%)316L tensile specimen and rod. (**E**) Enlarged BSE image showing the lava-like heterogeneous microstructure with the coexistence of acicular α′ martensite (yellow arrows) and ultrafine β grains with solidification cellular structure (blue arrows). (**F**) Fine acicular α′ martensite as observed by TEM bright-field image. (**G**) Ultrafine twin structure as observed by TEM bright-field image. (**H** and **I**) EBSD images of as-printed Ti64-(4.5%)316L. (**H**) Band contrast image of side-view cross section showing the ultrafine grain structure without columnar grains. The bright regions (blue arrows) consist of bulk β grains, and the dark regions (yellow arrows) consist of fine acicular α′ martensite. (**I**) Inverse pole figure (IPF) map of the top-view cross section showing grain orientations of β and α′ phases.

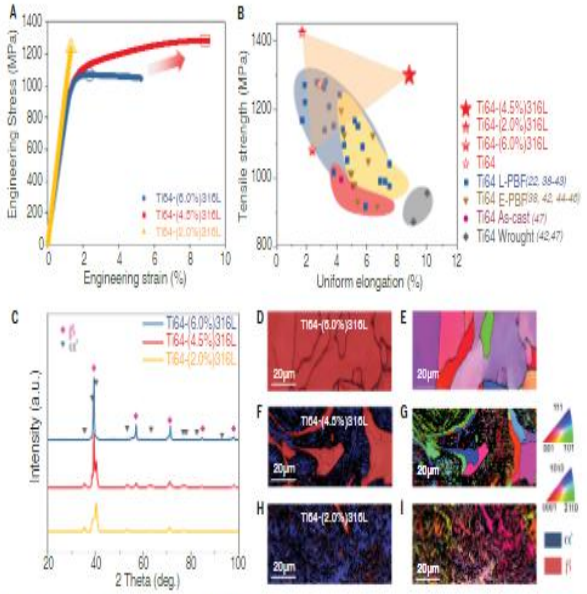

**Fig. 2. Microstructure and mechanical properties of the as-printed microCM Ti64-x316L alloy.** (**A**) Engineering stress-strain curves of as-printed Ti64-(6.0%)316L, Ti64-(4.5%)316L, and Ti64-(2.0%)316L alloys, respectively. The UTS is marked by big open symbols in the curves. (**B**) Engineering tensile strength versus uniform elongation of the as-printed Ti64-x316L alloy as compared with Ti64 alloy produced by different AM methods and conventional technologies (*22*, *38*–*47*). (**C** to **I**) Influence of microCMs on microstructure of Ti64-x316L alloys. (**C**) XRD profiles of phase constitution of three alloys. a.u., arbitrary units. [(**D**) to (**I**)] EBSD phase images and IPF maps of three different as-printed alloys showing phase constituents and grain orientations.

[4] **Toughening hydrogels through force-triggered chemical reactions that lengthen polymer strands**

**通过延长聚合物链的力引发化学反应，增韧水凝胶**

**出版信息：**SCIENCE 8 Oct 2021，Vol 374, Issue 6564，pp. 193-196

**作者：**ZI WANG, XUJUN ZHENG, TETSU OUCHI, TATIANA B. KOUZNETSOVA, HALEY K. BEECH, SARAH AV-RON, ET AL.

**第一作者单位：**Department of Chemistry, Duke University, Durham, NC,USA.

**全文链接：**https://www.science.org/doi/10.1126/science.abg2689

Abstract：

The utility and lifetime of materials made from polymer networks, including hydrogels, depend on their capacity to stretch and resist tearing. In gels and elastomers, those mechanical properties are often limited by the covalent chemical structure of the polymer strands between cross-links, which is typically fixed during the material synthesis. We report polymer networks in which the constituent strands lengthen through force-coupled reactions that are triggered as the strands reach their nominal breaking point. In comparison with networks made from analogous control strands, reactive strand extensions of up to 40% lead to hydrogels that stretch 40 to 50% further and exhibit tear energies that are twice as large. The enhancements are synergistic with those provided by double-network architectures and complement other existing toughening strategies.

**摘要翻译：**

由聚合物网络制成的材料（包括水凝胶）的效用和寿命取决于它们的拉伸和抗撕裂能力。在凝胶和弹性体中，这些机械性能通常受到交联聚合物链的共价化学结构的限制，这通常在材料合成过程中固定。

研究组报告了聚合物网络，其中组成链通过力耦合反应延长，当链达到其标称断裂点时被触发。与由类似控制链制成的网络相比，高达 40%的反应链延伸导致水凝胶进一步拉伸 40%至 50%，并显示出两倍大的撕裂能。

这些增强与双网络体系结构提供的增强具有协同作用，并补充了其他现有的增韧策略。

**文中插图：**

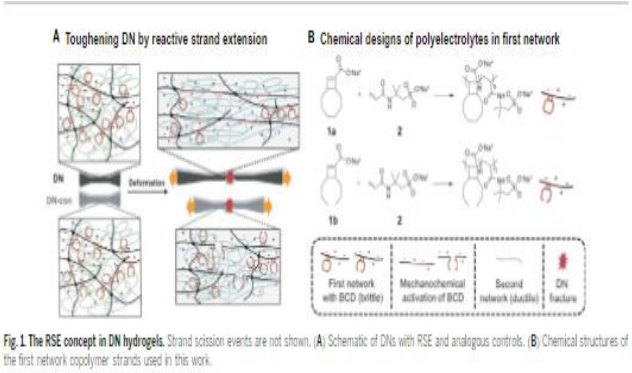


**Fig. 1. The RSE concept in DN hydrogels.** Strand scission events are not shown. (**A**) Schematic of DNs with RSE and analogous controls. (**B**) Chemical structures of the first network copolymer strands used in this work.

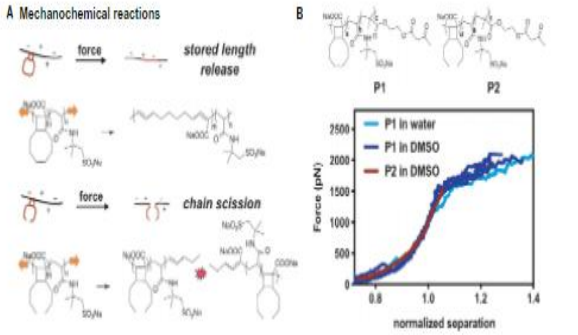


**Fig. 2. Mechanochemical reactions driving RSE.** (**A**) Mechanically coupled [2+2] cycloreversion leads to chain extension in BCD mechanophores and to chain scission in analogous acyclic cyclobutane mechanophores. (**B**) Representative single-molecule force-extension curves of linear RSE copolymer **P1** in water and dimethyl sulfoxide (DMSO), and control copolymer **P2** in DMSO.

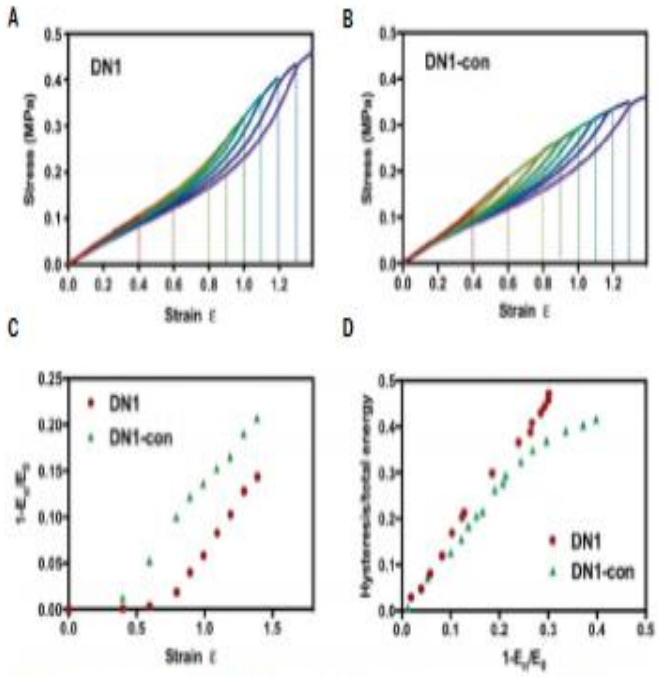


**Fig. 4. Hysteresis analysis of DN1 and DN1-con.** (**A** and **B**) Cyclic loading-unloading of (A) **DN1** and (B) **DN1-con** in small strain range. (**C**) Fractional loss of Young's modulus of **DN1** and **DN1-con** as a function of strain. (**D**) Fractional hysteresis as a function of fractional loss in modulus for **DN1** and **DN1-con**.

[5] **Broadband electro-optic polarization conversion with atomically thin black phosphorus**

**原子薄黑磷的宽带电光偏振转换**

**出版信息：**SCIENCE 22 Oct 2021，Vol 374, Issue 6566，pp. 448-453

**作者：**SOUVIK BISWAS, MEIR Y. GRAJOWER, KENJI WATANABE et al.

**第一作者单位：**Thomas J. Watson Laboratory of Applied Physics, CaliforniaInstitute of Technology, Pasadena, CA 91125, USA.

**全文链接：**https://www.science.org/doi/10.1126/science.abj7053

**Abstract：**

Active polarization control is highly desirable in photonic systems but has been limited mostly to discrete structures in bulky dielectric media and liquid crystal–based variable retarders. Here, we report electrically reconfigurable polarization conversion across telecommunication wavelengths (1410 to 1575 nanometers) in van der Waals layered materials using tri-layer black phosphorus (TLBP) integrated in a Fabry-Pérot cavity. The large electrical tunability of birefringence in TLBP enables spectrally broadband polarization control. We found that polarization states could be generated over a large fraction of the Poincaré sphere through spectral tuning, and that electrical tuning enables the state of polarization conversion to span nearly half the Poincaré sphere. We observed both linear to circular and cross-polarization conversion with voltage, demonstrating versatility with a high dynamic range.

**摘要翻译：**

有源偏振控制在光子系统中是非常理想的，但主要局限于大体积介质中的离散结构和基于液晶的可变延迟器。

在次，我们报道利用集成在法布里－珀罗腔中的三层黑磷（TLBP）在范德华层状材料中通过通信波长（1410 到 1575 纳米）的电可重构极化转换。TLBP 中双折射的大电可调谐性使得光谱宽带偏振控制成为可能。

我们发现，通过光谱调谐，可以在庞加莱球体的很大一部分产生极化状态，而电调谐使极化转换的状态跨越了庞加莱球体的近一半。我们观察了线性到圆形和交叉极化电压转换，证明了高动态范围的通用性。

**文中插图：**

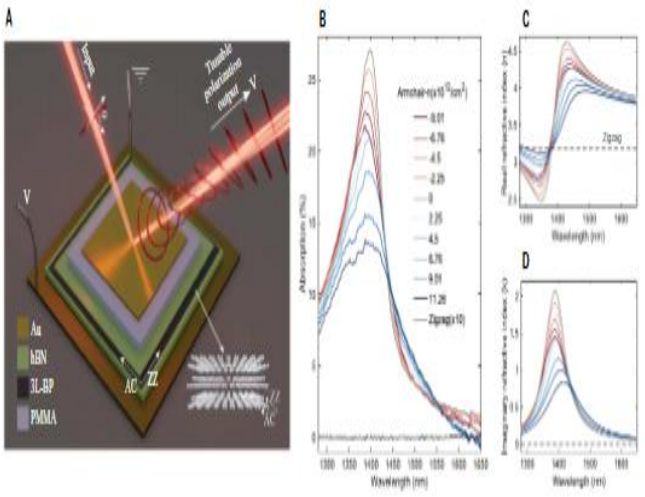


**Fig. 1. Schematic of electrically tunable polarization conversion and TLBP birefringence.** (**A**) Schematic of cavity design and polarization conversion. TLBP is incorporated in a dielectric environment between two mirrors [one partially reflective (top) and one highly reflective (bottom)]. The incoming beam is linearly polarized, and the output beam can be azimuthally rotated or converted between circular and linear polarization with applied voltage (between the TLBP and the back electrode or mirror) for a fixed wavelength. (**B**) Experimentally measured polarized absorption from a TLBP device (non-cavity-integrated) for different doping densities along the AC direction. The ZZ direction remains featureless for all conditions. (**C** and **D**) Extracted complex refractive index (real and imaginary part, respectively) for TLBP as a function of doping density for the AC and ZZ directions.

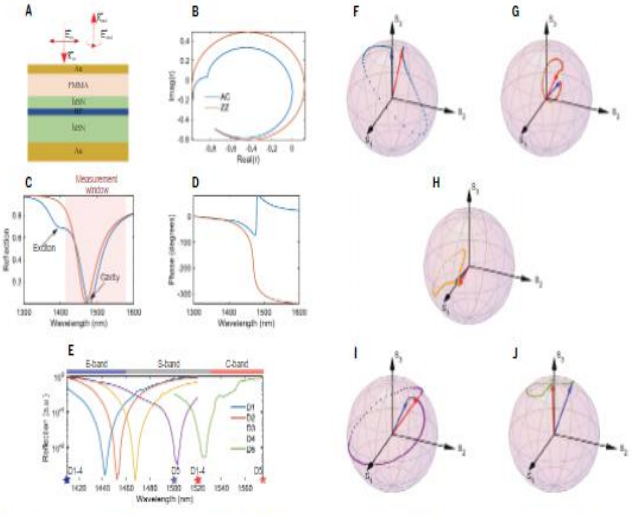


**Fig. 2. Example cavity design for polarization conversion and large anisotropy bandwidth experimental demonstration.** (**A**) Side view of a typical cavity structure adopted in this work. The top and bottom mirrors are formed by thin and thick Au films, respectively. The cavity is composed of hBN-encapsulated TLBP and PMMA, which act as the tunable part in determining the resonance wavelength. (**B** to **D**) Theoretically calculated complex reflection phasor, reflection amplitude, and phase spectrum, respectively, for such a typical cavity structure having resonance ~1480 nm, showing differences in both parameters along AC and ZZ and thus establishing polarization conversion. (**E**) Summary of reflection amplitude spectra from five representative devices fabricated as part of this study showing tunable cavity resonance. The PMMA thickness was tuned systematically to change the resonance over 90 nm across the tele-communication band (E, S, and C). (**F** to **J**) Experimentally measured spectral trajectories on the normalized Poincaré sphere corresponding to the five device resonances plotted in (E). All trajectories show strong spectral polarization conversion (either in the azimuthal orientation or the ellipticity or both). The differences in the trajectories are intimately related to the critical coupling between the cavity and the incoming polarization. For all presented trajectories, the azimuthal orientation was aligned nearly 45 degrees to the AC and ZZ direction of the TLBP flake. For each normalized Poincaré sphere, the blue arrows mark the beginning of the spectral scan (1410 nm for D1 to D4, 1500 for D5) and the red arrows mark the end (1520 nm for D1 to D4, 1575 for D5), also shown as stars in *x*-axis of (E).

[6] **Microscopic evolution of doped Mott insulators from polaronic metal to Fermi liquid**

**掺杂莫特绝缘体，从极化金属到费米液体微观演化**

**出版信息：**SCIENCE 1 Oct 2021，Vol 374, Issue 6563，pp. 82-86

**作者：**JOANNIS KOEPSELL, DOMINIK BOURGUND, PIMONPAN SOMPET et al.

**第一作者单位：**Max-Planck-Institut für Quantenoptik, 85748 Garching,Germany

**全文链接：**https://www.science.org/doi/10.1126/science.abe7165

**Abstract：**

The competition between antiferromagnetism and hole motion in two-dimensional Mott insulators lies at the heart of a doping-dependent transition from an anomalous metal to a conventional Fermi liquid. We observe such a crossover in Fermi-Hubbard systems on a cold-atom quantum simulator and reveal the transformation of multipoint correlations between spins and holes upon increasing doping at temperatures around the superexchange energy. Conventional observables, such as spin susceptibility, are furthermore computed from the microscopic snapshots of the system. Starting from a magnetic polaron regime, we find the system evolves into a Fermi liquid featuring incommensurate magnetic fluctuations and fundamentally altered correlations. The crossover is completed for hole dopings around 30%. Our work benchmarks theoretical approaches and discusses possible connections to lower-temperature phenomena.

**摘要翻译：**

在二维莫特绝缘体中，反铁磁性和空穴运动之间的竞争是反常金属到传统费米液体掺杂依赖转变的核心。我们在冷原子量子模拟器上观察到费米-哈伯德系统中的这种自旋转变，揭示了在超交换能周围温度下，随着掺杂的增加，自旋和空穴之间的多点相关性发生了转变。

常规的观测值，如自旋磁化率，是进一步从系统的微观快照中计算出来的。从磁极化子体系开始，我们发现系统演化为具有不相称磁涨落和根本改变相关性的费米液体。孔洞掺杂约 30%的交叉完成。我们的工作以理论方法为基准，并讨论了与低温现象的可能联系。

**文中插图：**

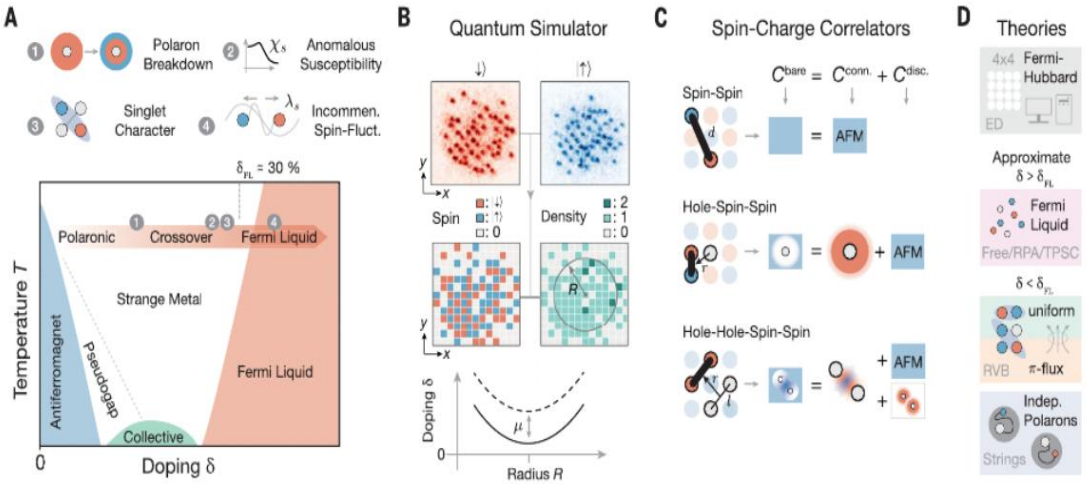


**Fig. 1. Probing doped Mott insulators with spin-charge correlators.** (**A**) Conjectured phase diagram of the 2D Fermi-Hubbard model upon hole doping δ and temperature *T*. Boundaries indicate crossovers between different regimes. Insets summarize our main experimental results. Incommen., incommensurate. (**B**) We independently image the two spin components of each Fermi-Hubbard realization with our quantum gas microscope. This enables reconstruction of the full spin and density (charge) information. The doping varies spatially in our harmonic trap and can be tuned by the total particle number to study the doping dependence of correlations. (**C**) Spin-spin, hole-spin-spin, and hole-hole-spin-spin correlators are analyzed in this work. As illustrated, bare multipoint correlations contain lower-order contributions and a connected part. For instance, in the magnetic polaron regime, a hole alters the antiferromagnetic environment in its vicinity. Therefore, bare hole-spin-spin correlations are reduced (white) close to the hole compared with the strong antiferromagnetic correlation at large distance (blue). The bare correlation ($C^{bare}$) can be decomposed into the genuine effect of the hole, that is, the connected part ($C^{conn.}$, red), and the antiferromagnetic (AFM) background value, that is, the disconnected part ($C^{disc.}$, blue). The sum of both parts corresponds to the bare correlation. Similarly, the genuine effect of a pair of holes on spin correlations (i.e., beyond single-hole effects) is quantified by the connected part of hole-hole-spin-spin correlations. This work focuses on connected correlations. (**D**) We compare experimental findings to exact diagonalization of 4×4 Fermi-Hubbard systems (top), mean-field–inspired approaches or free fermions approximating Fermi liquids at high doping (second from top), as well as three approaches (uniform-RVB, π-flux, and string), which are designed to capture the low-doping regime (bottom two panels). Indep., independent.

[7] **High-strength scalable MXene films through bridging-induced densification**

**通过桥联致密化的高强度可扩展 MXene 薄膜**

**出版信息：**SCIENCE 1 Oct 2021，Vol 374, Issue 6563，pp. 96-99

**作者：**SIJIE WAN, XIANG LI, YING CHEN et al.

**第一作者单位：**School of Chemistry, Key Laboratory of Bio-inspired Smart Interfacial Science and Technology of Ministry of Education, Beijing Advanced Innovation Center for Biomedical Engineering, BeihangUniversity, Beijing 100191, P. R. China.

**全文链接：**https://www.science.org/doi/10.1126/science.abg2026

**国内相关报道：**http://news.buaa.edu.cn/info/1002/54814.htm

**Abstract：**

MXenes are a growing family of two-dimensional transition metal carbides and/or nitrides that are densely stacked into macroscopically layered films and have been considered for applications such as flexible electromagnetic interference (EMI) shielding materials. However, the mechanical and electrical reliabilities of titanium carbide MXene films are affected by voids in their structure. We applied sequential bridging of hydrogen and covalent bonding agents to induce the densification of MXene films and removal of the voids, leading to highly compact MXene films. The obtained MXene films show high tensile strength, in combination with high toughness, electrical conductivity, and EMI shielding capability. Our high-performance MXene films are scalable, providing an avenue for assembling other two-dimensional platelets into high-performance films.

**摘要翻译：**

MXenes 是一个不断发展的二维过渡金属碳化物和/或氮化物家族，它们被密集地堆积成宏观层状薄膜，已被考虑用于柔性电磁干扰（EMI）屏蔽材料等。然而，碳化钛 MXene 薄膜的机械和电气可靠性受到其结构中的孔隙的影响。我们利用氢键和共价键合剂的顺序桥联诱导 MXene 薄膜的致密化和孔隙的去除，导致高度致密的 MXene 薄膜。所得的 MXene 薄膜具有较高的抗拉强度，同时具有较高的韧性、导电性和 EMI 屏蔽性能。我们的高性能 MXene 薄膜是可扩展的，为将其他二维薄片组装成高性能薄膜提供了途径。

**文中插图：**

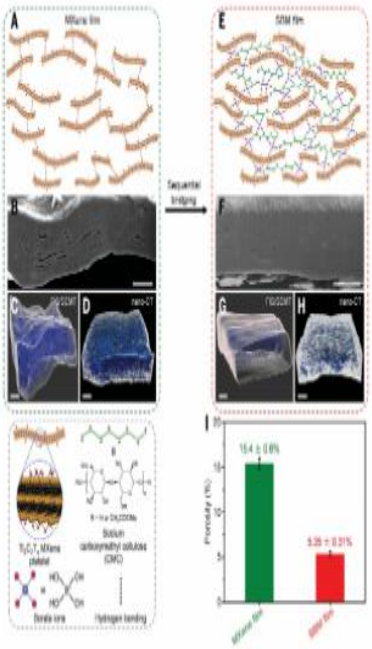

**Fig. 1. Structural characterization of SBM films.** (**A** and **E**) Structural models of MXene (A) and SBM (E) films. (**B** and **F**) SEM images of cross-sections cut by an FIB for MXene (B) and SBM (F) films. (**C** and **G**) 3D-reconstructed void microstructure derived from FIB/SEMT for MXene (C) and SBM (G) films. Note that the serial section derived from FIB/SEMT is not perpendicular to the film surface. (**D** and **H**) 3D-reconstructed void microstructure derived from nano-CT for MXene (D) and SBM (H) films. Scale bars, 2 μm. (**I**) Porosities of MXene and SBM films derived from density measurements.

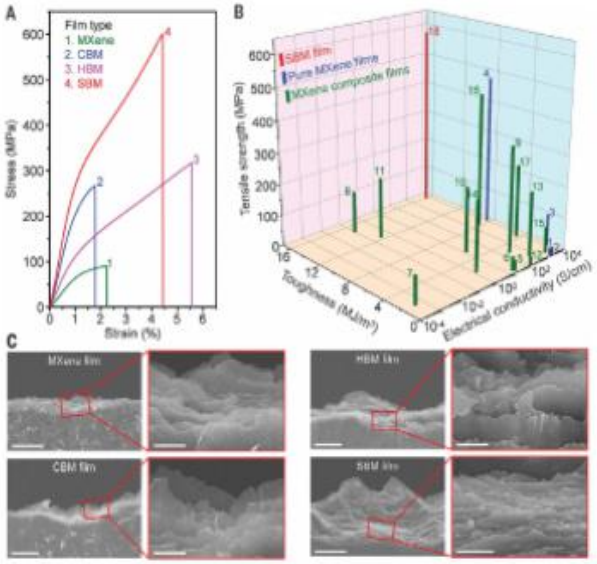

**Fig. 2. Mechanical properties of SBM films.** (**A**) Representative tensile stress–strain curves of MXene, CBM, HBM, and SBM films. (**B**) Comparison of the tensile strength, toughness, and electrical conductivity of SBM films (red line) with those of previously reported pure MXene films (blue lines) and MXene composite films (green lines). (**C**) Inclined-view SEM images of the fracture surfaces of MXene, CBM, HBM, and SBM films. Scale bars, 5 μm in low-resolution images and 1 μm in high-resolution images.

[8] **Ultrahigh energy storage in superparaelectric relaxor ferroelectrics**

**超顺电弛豫铁电体中的超高能量存储**

**出版信息：**SCIENCE 1 Oct 2021，Vol 374, Issue 6563，pp. 100-104

**作者：**HAO PAN, SHUN LAN, SHIQI XU et al.

**第一作者单位：**State Key Laboratory of New Ceramics and Fine Processing,School of Materials Science and Engineering, TsinghuaUniversity

**全文链接：**https://www.science.org/doi/10.1126/science.abi7687

**国内相关报道：**https://www.mse.tsinghua.edu.cn/info/1062/2020.htm

**Abstract：**

Electrostatic energy storage technology based on dielectrics is fundamental to advanced electronics and high-power electrical systems. Recently, relaxor ferroelectrics characterized by nanodomains have shown great promise as dielectrics with high energy density and high efficiency. We demonstrate substantial enhancements of energy storage properties in relaxor ferroelectric films with a superparaelectric design. The nanodomains are scaled down to polar clusters of several unit cells so that polarization switching hysteresis is nearly eliminated while relatively high polarization is maintained. We achieve an ultrahigh energy density of 152 joules per cubic centimeter with markedly improved efficiency (>90% at an electric field of 3.5 megavolts per centimeter) in superparaelectric samarium-doped bismuth ferrite–barium titanate films. This superparaelectric strategy is generally applicable to optimize dielectric and other related functionalities of relaxor ferroelectrics.

**摘要翻译：**

基于电介质的静电储能技术是先进电子技术和大功率电气系统的基础。近年来，以纳米结构为特征的弛豫铁电体作为高能量密度、高效率的电介质，展现出广阔的应用前景。

我们用超顺电的设计证明了弛豫铁电薄膜的储能性能的显著增强。纳米域被缩小到由几个单元细胞组成的极性簇，从而在保持较高极化的同时几乎消除了极化切换滞。

我们在超顺电 Sm 掺杂铁酸铋-钛酸钡薄膜中实现了 152 焦耳/立方厘米的超高能量储存密度，并显著提高了效率（在 3.5 兆伏/厘米的电场下超过了 90%）。这种超顺电策略一般适用于优化弛豫铁电体的介电和其他相关功能。

**文中插图：**

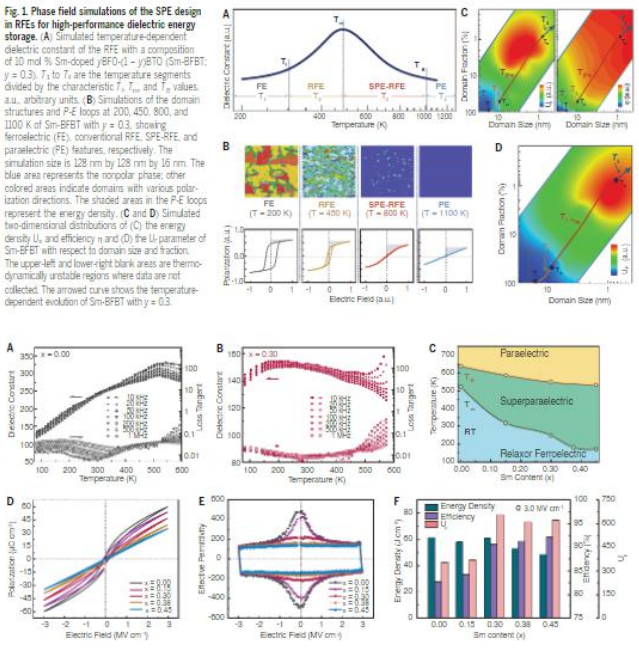

**Fig. 1. Phase field simulations of the SPE design in RFEs for high-performance dielectric energy storage.** (**A**) Simulated temperature-dependent dielectric constant of the RFE with a composition of 10 mol % Sm-doped yBFO-(1 − y)BTO (Sm-BFBT; y = 0.3). $T_1$ to $T_4$ are the temperature segments divided by the characteristic $T_c$, $T_m$, and $T_R$ values. a.u., arbitrary units. (**B**) Simulations of the domain structures and *P*-*E* loops at 200, 450, 800, and 1100 K of Sm-BFBT with y = 0.3, showing ferroelectric (FE), conventional RFE, SPE-RFE, and paraelectric (PE) features, respectively. The simulation size is 128 nm by 128 nm by 16 nm. The blue area represents the nonpolar phase; other colored areas indicate domains with various polarization directions. The shaded areas in the *P*-*E* loops represent the energy density. (**C** and **D**) Simulated two-dimensional distributions of (C) the energy density $U_e$ and efficiency η and (D) the $U_r$ parameter of Sm-BFBT with respect to domain size and fraction. The upper-left and lower-right blank areas are thermodynamically unstable regions where data are not collected. The arrowed curve shows the temperature-dependent evolution of Sm-BFBT with y = 0.3.



**Fig. 2. Dielectric, polarization, and energy storage properties of the Sm-BFBT films.** (**A** and **B**) Temperature-dependent dielectric spectra for (A) *x* = 0 and (B) *x* = 0.30. (**C**) Phase diagram of the Sm-BFBT films with respect to temperature and Sm content *x*. RT denotes room temperature. $T_m$ values are derived from the dielectric spectra at 1 MHz. $T_R$ values are from SHG measurements. (**D**) *P*-*E* loops at an electric field of 3.0 MV cm$^{-1}$ and 5 kHz. (**E**) Field-dependent effective permittivity of the Sm-BFBT films. (**F**) Comparison of energy density, efficiency and $U_r$ (unit: Joules per cubic centimeter) of the Sm-BFBT films at 3.0 MV cm$^{-1}$.

nonlinearity and relatively high $P_m$ (Fig. 1B), thus achieving the best compromise for energy storage.

To quantitatively evaluate the trade-off between high polarization (large $U_e$) and low hysteresis (low $U_{loss}$, and thus high η) for high overall energy storage performance, we defined a parameter $U_r = U_e\eta(1 - \eta)$. From the simulated *P*-*E* loops of Sm-BFBT (fig. S4), we derived the $U_e$ and η values and calculated $U_r$. We displayed $U_e$, η, and $U_r$ as two-dimensional distributions for the domain size and fraction (Fig. 1, C and D). We found that a high $U_e$ could be attained with moderate domain sizes of 1 to 10 nm and moderate domain fractions of 0.5 to 8%, whereas η is monotonously increased with reduced domain size and fraction. The area with high $U_r$ is thus driven to the ranges with a domain size of ~2 nm (two to five unit cells for the perovskite Sm-BFBT) and domain fraction of ~0.5 to 5%, which are

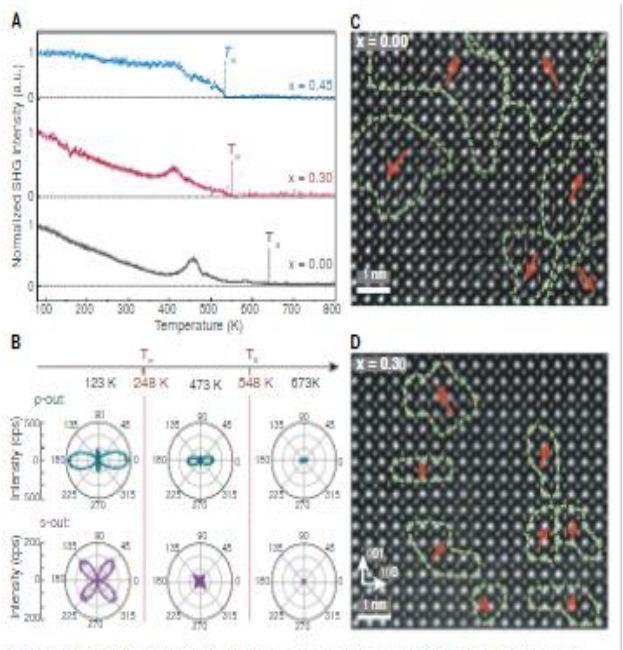

**Fig. 3. Microstructural origins of the SPE.** (**A**) Temperature-dependent SHG intensity (with the *p*-in and *p*-out configuration) of the Sm-BFBT films with *x* = 0, 0.30, and 0.45. (**B**) SHG patterns with the *p*-out and *s*-out configurations for *x* = 0.30 at 123, 473, and 673 K, corresponding to the RFE ($<T_m$), SPE ($T_m < T < T_R$), and paraelectric ($>T_R$) segments, respectively. Dots represent experimental data; lines represent fittings. (**C** and **D**) HAADF STEM images for (C) *x* = 0 and (D) *x* = 0.30. Brown arrows show B-site cation displacement vectors in each unit cell; green dashed lines delineate domain areas, in which red arrows denote the orientation of the collective B-site cation displacement of the domains.

[1] **Half- and quarter-metals in rhombohedral trilayer graphene**

**菱面体三层石墨烯中的半金属和四分之一金属**

**出版信息：**Nature volume 598, pages429–433 (2021)

**作者：**Haoxin Zhou, Tian Xie, Areg Ghazaryan, Tobias Holder, James R. Ehrets, Eric M. Spanton, et al.

**第一作者单位：**Department of Physics, University of California, Santa Barbara, CA, USA

**全文链接：**https://www.nature.com/articles/s41586-021-03938-w

**Abstract:**

Ferromagnetism is most common in transition metal compounds where electrons occupy highly localized d orbitals. However, ferromagnetic order may also arise in low-density two-dimensional electron systems. Here we show that gate-tuned van Hove singularities in rhombohedral trilayer graphene drive spontaneous ferromagnetic polarization of the electron system into one or more spin and valley flavours. Using capacitance and transport measurements, we observe a cascade of transitions tuned to the density and electronic displacement field between phases in which quantum oscillations have fourfold, twofold or onefold degeneracy, associated with a spin- and valley-degenerate normal metal, spin-polarized ‘half-metal’, and spin- and valley-polarized ‘quarter-metal’, respectively. For electron doping, the salient features of the data are well captured by a phenomenological Stoner model that includes valley-anisotropic interactions. For hole filling, we observe a richer phase diagram featuring a delicate interplay of broken symmetries and transitions in the Fermi surface topology. Finally, we introduce a moiré superlattice using a rotationally aligned hexagonal boron nitride substrate. Remarkably, we find that the isospin order is only weakly perturbed, with the moiré potential catalysing the formation of topologically nontrivial gapped states whenever itinerant half- or quarter-metal states occur at half- or quarter-superlattice band filling. Our results show that rhombohedral graphene is an ideal platform for well-controlled tests of many-body theory, and reveal magnetism in moiré materials to be fundamentally itinerant in nature.

**摘要翻译：**

铁磁性在电子占据高度局域化 d 轨道的过渡金属化合物中最为常见。然而，在低密度二维电子系统中也可能出现铁磁有序。研究组证明了菱面体三层石墨烯中的门调谐范霍夫奇点，驱动电子系统的自发铁磁极化转变为一种或多种自旋和谷型。通过电容和输运测量，研究组观察到调谐至相位间载流子浓度和电位移场的一系列跃迁，其中量子振荡具有四重、二重或一重简并度，分别对应自旋和谷简并的“正常金属态”、自旋极化的“半金属态”以及自旋极化和谷极化的“四分之一金属态”。对于电子掺杂，包含谷各向异性相互作用的唯象斯通纳模型很好地捕捉到了数据的显著特征。对于空穴填充，研究组观察到一个更丰富的相图，其特征是费米面拓扑中对称性破缺和跃迁的微妙相互作用。最后，研究组通过旋转对齐的六方氮化硼衬底引入莫尔超晶格。值得注意的是，研究组发现同位旋序仅受到弱扰动，当迁移的半金属态或四分之一金属态填充半超晶格带或四分之一超晶格带时，莫尔势会催化拓扑非平凡间隙态的形成。该结果表明，菱面体石墨烯是一个多体理论控制测试的理想平台，并揭示了莫尔材料的磁性本质上是迁移的。

**文中插图：**

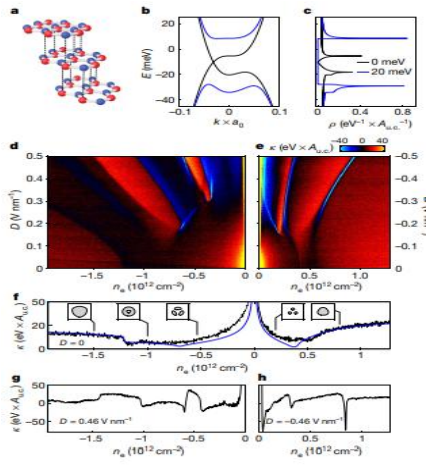

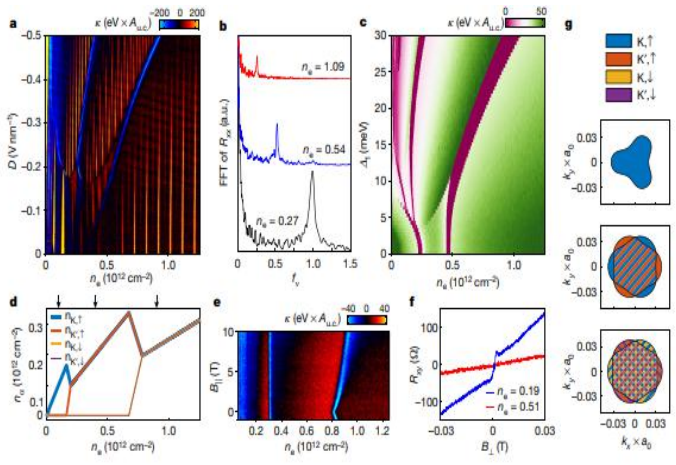

[2] **Superconductivity in rhombohedral trilayer graphene**

**菱面体三层石墨烯的超导性**

**出版信息：**Nature volume 598, pages434–438 (2021)

**作者：**Haoxin Zhou, Tian Xie, Takashi Taniguchi, Kenji Watanabe & Andrea F. Young.

**第一作者单位:** Department of Physics, University of California, Santa Barbara, CA, USA.

**全文链接：**https://www.nature.com/articles/s41586-021-03926-0

**Abstract:**

To access superconductivity via the electric field effect in a clean, two-dimensional device is a central goal of nanoelectronics. Recently, superconductivity has been realized in graphene moiré heterostructures; however, many of these structures are not mechanically stable, and experiments show signatures of strong disorder. Here we report the observation of superconductivity—manifesting as low or vanishing resistivity at sub-kelvin temperatures—in crystalline rhombohedral trilayer graphene, a structurally metastable carbon allotrope. Superconductivity occurs in two distinct gate-tuned regions (SC1 and SC2), and is deep in the clean limit defined by the ratio of mean free path and superconducting coherence length. Mapping of the normal state Fermi surfaces by quantum oscillations reveals that both superconductors emerge from an annular Fermi sea, and are proximal to an isospin-symmetry-breaking transition where the Fermi surface degeneracy changes. SC1 emerges from a paramagnetic normal state, whereas SC2 emerges from a spin-polarized, valley-unpolarized half-metal and violates the Pauli limit for in-plane magnetic fields by at least one order of magnitude. We discuss our results in view of several mechanisms, including conventional phonon-mediated pairing, pairing due to fluctuations of the proximal isospin order, and intrinsic instabilities of the annular Fermi liquid. Our observation of superconductivity in a clean and structurally simple two-dimensional metal provides a model system to test competing theoretical models of superconductivity without the complication of modelling disorder, while enabling new classes of field-effect controlled electronic devices based on correlated electron phenomena and ballistic electron transport.

**摘要翻译:**

在一个干净的二维器件中通过电场效应获得超导性是纳米电子学的一个核心目标。最近，石墨烯莫尔异质结构已实现超导性；然而，其中许多结构在机械上并不稳定，实验显示出强无序特征。研究组报道了在亚开尔文温度下表现为低电阻率或零电阻率的晶体菱面三层石墨烯（一种结构上亚稳态的碳同素异形体）的超导性。超导性发生在两个不同的门调谐区（SC1 和 SC2），且深度在由平均自由程和超导态相干长度之比定义的干净极限内。量子振荡对常态费米面的映射显示，这两种超导体都来自环形费米海，并且接近同位旋对称性破缺转变，其中费米面简并度发生变化。SC1 从顺磁正常态出现，而 SC2 则从自旋极化、谷简并的半金属态中出现，且违反了面内磁场的泡利极限至少一个数量级。研究组讨论了该结果的各种机制，包括传统的声子介导配对，近同位旋序波动产生的配对，以及环形费米液体的固有不稳定性导致的配对。研究组为干净且结构简单的二维金属中超导性的观察提供了一个模型系统，用于测试相互竞争的超导理论模型，而不会出现建模混乱的复杂情况，同时使基于相关电子现象和弹道电子输运的新型场效应控制电子器件成为可能。

**文中插图：**

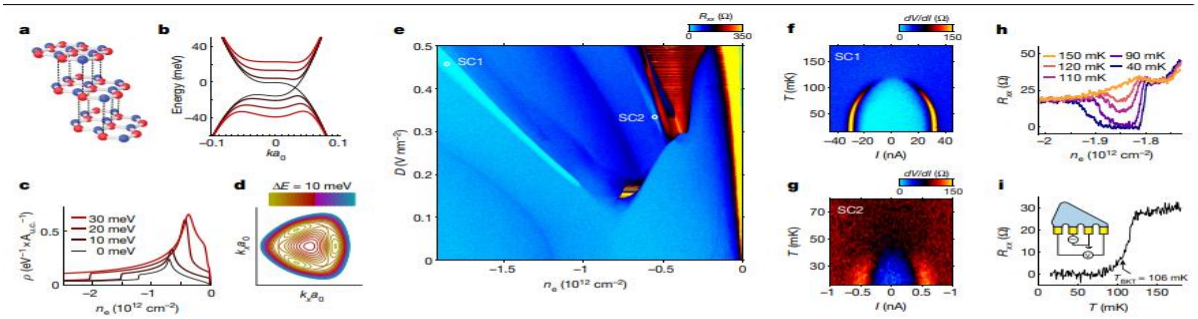


**Fig. 1 | Superconductivity in RTG. a**, Crystal structure of RTG. **b**, Band structure of RTG for interlayer potential $\Delta_1 = 0, 10, 20$ and 30 meV. **c**, Density of states, $\rho$, calculated in the single particle model. $A_{u.c.}$ is the area of the RTG unit cell (u.c.). **d**, Isoenergetic contours near the valence band maximum for $\Delta_1 = 20$ meV plotted over a range of $-0.08 < k_{x,y}a_0 < 0.08$. Contours span a range of energy of 10 meV. **e**, Resistivity as a function of electron density $n_e$ and perpendicular displacement field $D$ measured with an 1 nA AC current at base temperature. **f**, **g**, Temperature and current dependence of the differential resistivity $dV/dI$ measured at the points in the $n_e - D$ plane indicated in **a**. **h**, Temperature-dependent resistivity across SC1 measured at $D = 0.46$ V nm$^{-1}$. **i**, $R_{xx}(T)$ corresponding to the data plotted in **f**. $T_{BKT} = 106$ mK. Inset, device schematic showing measurement configuration $R_{xx}$.

[3] **Dexterous magnetic manipulation of conductive non-magnetic objects**

**导电非磁性物体的灵巧磁操控**

**出版信息：**Nature volume 598, pages439–443 (2021)

**作者：**Lan N. Pham, Griffin F. Tabor, Ashkan Pourkand, Jacob L. B. Aman, Tucker Hermans & Jake J. Abbott.

**第一作者单位：**Department of Mechanical Engineering, University of Utah, Salt Lake City, UT, USA.

**全文链接：**https://www.nature.com/articles/s41586-021-03966-6

**Abstract：**

Dexterous magnetic manipulation of ferromagnetic objects is well established, with three to six degrees of freedom possible depending on object geometry. There are objects for which non-contact dexterous manipulation is desirable that do not contain an appreciable amount of ferromagnetic material but do contain electrically conductive material. Time-varying magnetic fields generate eddy currents in conductive materials, with resulting forces and torques due to the interaction of the eddy currents with the magnetic field. This phenomenon has previously been used to induce drag to reduce the motion of objects as they pass through a static field, or to apply force on an object in a single direction using a dynamic field, but has not been used to perform the type of dexterous manipulation of conductive objects that has been demonstrated with ferromagnetic objects. Here we show that manipulation, with six degrees of freedom, of conductive objects is possible by using multiple rotating magnetic dipole fields. Using dimensional analysis, combined with multiphysics numerical simulations and experimental verification, we characterize the forces and torques generated on a conductive sphere in a rotating magnetic dipole field. With the resulting model, we perform dexterous manipulation in simulations and physical experiments.

**摘要翻译：**

对铁磁物体的灵巧磁操控已很好建立，根据物体的几何结构，可能有三到六个自由度。有些物体需要非接触式灵巧操作，它们不含有大量的铁磁性材料，但含有导电材料。时变磁场在导电材料中产生涡流，涡流与磁场相互作用产生力和力矩。这种现象曾被用于诱导阻力，以减少物体通过静态场时的运动，或使用动态场在单个方向上对物体施加力，但尚未被用于对导电物体进行如铁磁物体那样的灵活操控。研究组表明，通过使用多个旋转磁偶极子场可在六个自由度下操控导电物体。利用量纲分析，结合多物理场数值模拟和实验验证，研究组描述了在旋转磁偶极子场中导电球体上产生的力和力矩。利用该模型，研究组在仿真和物理实验中实现了灵活操控。

**文中插图：**

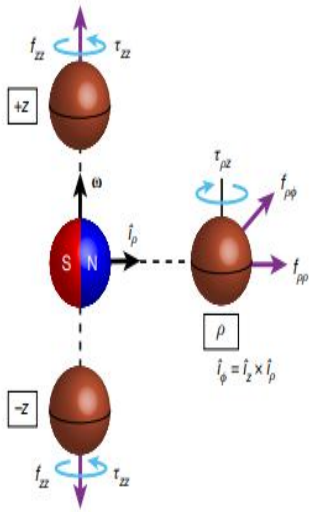


**Fig. 1 | Induced forces and torques on a conductive sphere in three canonical positions relative to a rotating magnetic dipole.** The dipole is spinning with angular velocity **ω**. Force and torque arrows are shown for all non-negligible components, with arrowheads depicting the actual directions corresponding to the **ω** shown.

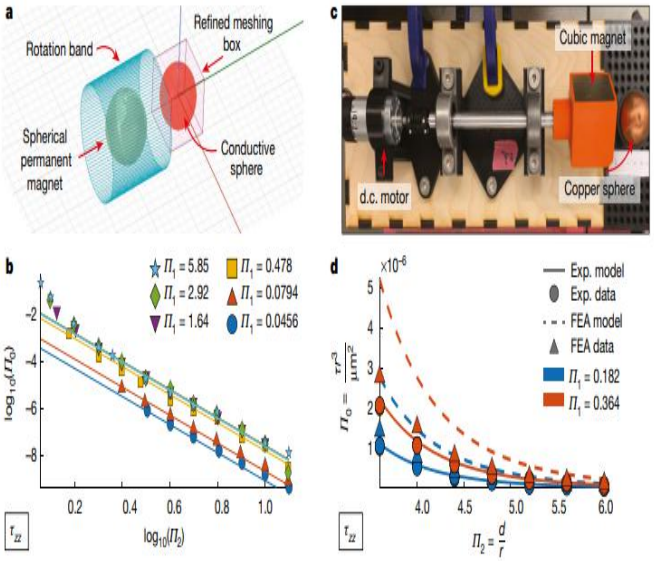


**Fig. 2 | Typical numerical and experimental results for force-torque characterization.** For clarity, only a subset of the data for a single component $\tau_{zz}$ is shown. **a**, Rendering of FEA simulation. **b**, FEA data with unified regression model. **c**, Top view of experimental set-up. **d**, Experimental data with unified regression model. Unified FEA regression model with new FEA data not included in the training set.